nature physics

ARTICLES

PUBLISHED ONLINE: 8 JUNE 2015 | DOI: 10.1038/NPHYS3341

Synchronous universal droplet logic and control

Georgios Katsikis[1], James S. Cybulski[1] and Manu Prakash[2]*

Droplets are versatile digital materials; they can be produced at high throughput, perform chemical reactions as miniature beakers and carry biological entities. Droplets have been manipulated with electric, optical, acoustic and magnetic forces, but all these methods use serial controls to address individual droplets. An alternative is algorithmic manipulation based on logic operations that automatically compute where droplets are stored or directed, thereby enabling parallel control. However, logic previously implemented in low-Reynolds-number droplet hydrodynamics is asynchronous and thus prone to errors that prevent scaling up the complexity of logic operations. Here we present a platform for error-free physical computation via synchronous universal logic. Our platform uses a rotating magnetic field that enables parallel manipulation of arbitrary numbers of ferrofluid droplets on permalloy tracks. Through the coupling of magnetic and hydrodynamic interaction forces between droplets, we developed AND, OR, XOR, NOT and NAND logic gates, fanouts, a full adder, a flip-flop and a finite-state machine. Our platform enables large-scale integration of droplet logic, analogous to the scaling seen in digital electronics, and opens new avenues in mesoscale material processing.

From Zuse's thesis[1], which pioneered digital physics, to Landauer[2] and Wheeler's famous 'it from bit'[3], we know that information is fundamentally linked to its physical representations; manipulation of information, for example, represented by the flow of electrons in a microcircuit[4] or biological molecules[5], intrinsically leads to algorithmic manipulation of matter. Although such algorithmic assembly is commonplace nowadays at the nanoscale, including DNA-based tile nanostructures[6,7], its counterpart at the mesoscale is surprisingly missing.

Droplets in microfluidic chambers are a growing platform for both physics[8,9] and biology experiments[10–12]. Several manipulation techniques, including electric[13–15], optical[16], acoustic[17] and magnetic[18] forces, have been used for serially manipulating droplets. Because these systems depend on external feedback by the user and lack any inherent computational capability, large scale-up and parallel information-based manipulation is limited. A simple assignment of presence or absence of a droplet as a bit of information can allow us to look at these multi-phase systems as information processing units. Recent work has demonstrated the universal computational capabilities of low-Reynolds-number multi-phase hydrodynamics using pressure-based flow controllers[19–22]. However, all of these prior systems suffer from a fundamental drawback; they are asynchronous and thus lack the capacity to scale to complex cascaded digital logic. To address this problem, we introduce a new platform that uses a single global clock—that is, a rotating magnetic field—to synchronize the motion of arbitrary numbers of ferrofluid droplets and direct or store them in permalloy tracks using digital logic operations. Through magnetic and hydrodynamic interaction forces between droplets, we developed OR/AND logic gates, universal XOR/AND and XOR/NAND gates, fanouts, memory loops, flip-flops, a finite-state machine and a full adder that adds droplet 'bits'. Our platform demonstrates both combinational and sequential logic and does not rely on pressure-based flow controllers, therefore enabling a unique 'non-volatile' conservative physical logic and memory.

The principle of operation of our platform relies on creating local energy minima or 'potential wells' on a planar (2D) Hele-Shaw flow geometry to set ferrofluid droplets in motion. For illustration, consider a 1D model of a droplet close to a moving potential well. Depending on the velocity of the well V_{well}, the droplet can either follow the well or fall behind it (Fig. 1a). Similarly, a droplet can follow a cascade of stationary wells that are time-varying and appear sequentially along a path. Although in a different physical system, a similar approach was developed as an early attempt to manipulate information via magnetic domains in garnet films in magnetic bubble technology[23]; we exploit this methodology to simultaneously manipulate both materials and information using universal logic. In the past, magnetophoretic approaches have been used to manipulate ferrofluid droplets[24] and, more recently, micrometre-scale colloidal particles[25,26]. These approaches lack the ability to implement logic gates. In contrast, our universal synchronous scheme implements logic gates by exploiting nonlinear magnetic and hydrodynamic interactions between fluid droplets. We developed a theoretical framework to understand this unique interplay of coupled magnetic and hydrodynamic forces on droplets. Moreover, we tested this framework by means of experiments and simulations to characterize the system's operational limits.

We create potential wells by patterning soft magnetic permalloy bars (Ni77/Fe14, 25 μm thickness) on a glass surface (Methods) and polarizing them using an in-plane rotating field $\mathbf{B}_{\mathrm{i}}$ ($B_{\mathrm{i}} = 20$–100 G). The droplets (diameters $d = 300$–$1{,}000$ μm) are also polarized out-of-plane by a static normal magnetic field $\mathbf{B}_{\mathrm{n}}$ ($B_{\mathrm{n}} = 100$–400 G). To minimize the magnetostatic energy U, each droplet is set in motion to match its south pole to the north pole of the bar that represents a potential well (Fig. 1b). We selected a periodic track of 'T-bars' and 'I-bars', owing to its geometric simplicity, from a rich design space of two-dimensional geometries[23]. When placed in a field $\mathbf{B}_{\mathrm{i}}$ with clockwise rotation, the 'T & I-bar' arrangement will produce a cascade, from left to right, of four potential wells per full rotation of $\mathbf{B}_{\mathrm{i}}$ (Fig. 1c). If $\mathbf{B}_{\mathrm{i}}$ has frequency f and a given track has spatial period S, droplets will be driven with an average speed $V_f = Sf$. Note that the permalloy bars exhibit low coercivity and negligible hysteresis (Supplementary Fig. 1a), enabling them to respond instantaneously to $\mathbf{B}_{\mathrm{i}}$. The fluidic chip (Fig. 1e) is placed inside an experimental set-up with Helmholtz coils that produce

[1]Department of Mechanical Engineering, Stanford University, 450 Serra Mall, California 94305, USA. [2]Department of Bioengineering, Stanford University, 450 Serra Mall, California 94305, USA. *e-mail: manup@stanford.edu

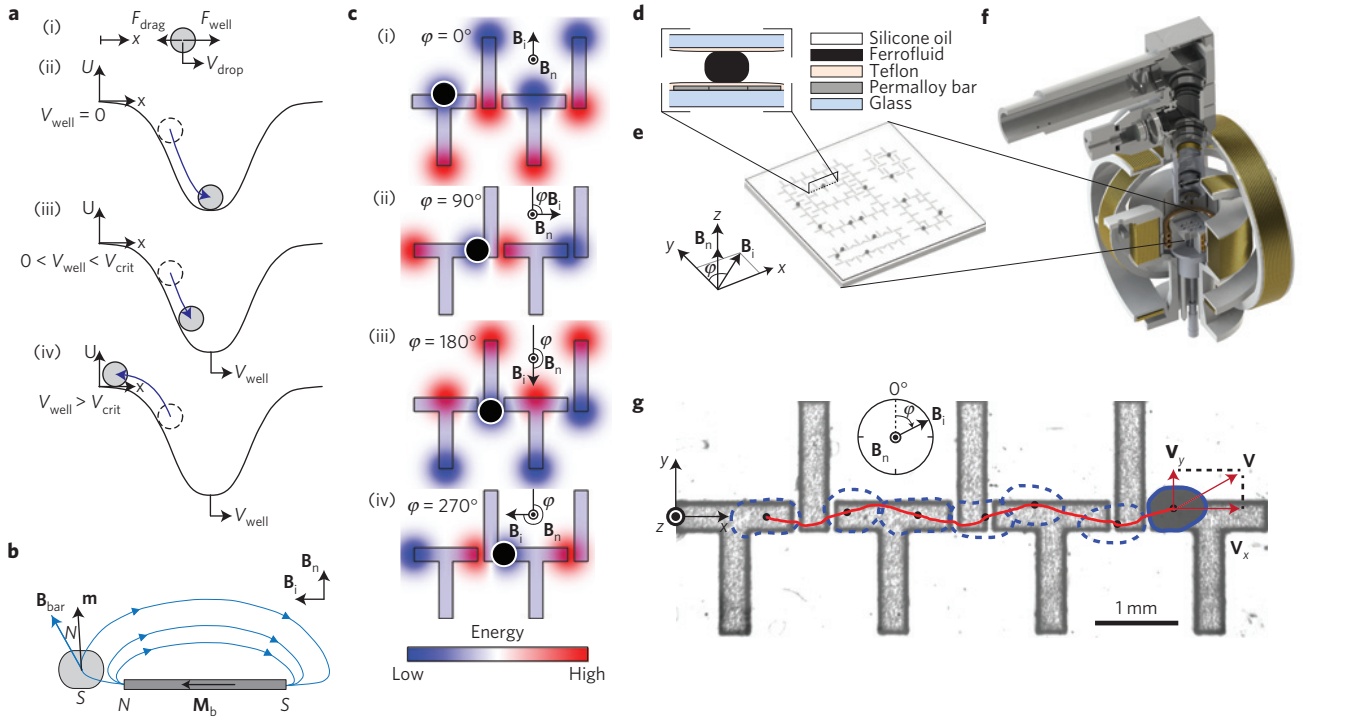

Figure 1 | Principle of operation and experimental set-up. a, (i) Free body diagram of a droplet with velocity V_{drop} in a 1D potential well $U(x)$ with velocity V_{well}, where $F_{well} = -dU/dx$ is the force due to the well and F_{drag} is the hydrodynamic force. (ii) Droplet equilibrium case $V_{well} = 0$: droplet settles at the centre of the well. (iii) $0 < V_{well} < V_{crit}$: droplet moves with the well $V_{drop} = V_{well}$ at a relative position where $F_{net} = F_{drag} + F_{well} = 0$. (iv) $V_{well} > V_{crit}$: droplet falls behind the well because V_{well} is higher than the critical V_{crit}, such that $F_{drag}(V_{crit}) > \max(F_{well})$. **b**, Schematic of a ferrofluid droplet with a magnetic dipole moment **m** (induced by a field $\mathbf{B}_n$) inside a field $\mathbf{B}_{bar}$ by a permalloy bar with magnetization $\mathbf{M}_b$ (induced by $\mathbf{B}_i$). The magnetostatic energy $U = -\mathbf{m} \cdot \mathbf{B}_{bar}$ is minimized when opposite poles of the droplet and the bars are paired. **c**, Schematic top view of droplet (shown as black dot) on '*T*-bars' and '*I*-bars'. During a full rotation of $\mathbf{B}_i$, the droplet follows the potential wells formed for each $\varphi = (0°, 90°, 180°, 270°)$, and thus moves rightwards. **d**, Schematic side view of Hele-Shaw geometry of a fluidic chip. **e**, Perspective view of a fluidic chip with magnetic fields $\mathbf{B}_i$, $\mathbf{B}_n$. **f**, Experimental set-up including electromagnetic coils combined with a microscope system. **g**, Video snapshot where a droplet propagates rightwards under a clockwise rotating field $\mathbf{B}_i$ and a fixed $\mathbf{B}_n$. The droplet trajectory is marked in red and the instantaneous droplet shapes are marked in blue dashed lines.

the magnetic fields $\mathbf{B}_n, \mathbf{B}_i$ and includes a high-speed camera (Fig. 1f, Methods and Supplementary Movie 1).

Experiments

We first developed a quantitative understanding of propagation circuits that act as simple wires in our logic scheme. We demonstrated synchronous droplet propagation of water-based ferrofluid droplets immersed in a oil-based carrier fluid between two parallel Teflon-coated glass surfaces (Fig. 1d). Single droplets with $d = 600\,\mu m$ were subjected to a field $\mathbf{B}_i$ in a frequency range $f = 3$–15 Hz. We also developed an image analysis code (Methods) and calculated the droplet positions and velocity components V_x and V_y (Fig. 1g).

Using the droplet diameter d as a tractable length scale, the Reynolds number exhibited an intermediate range[27] $\mathrm{Re} \sim 1$–10, ($\mathrm{Re} = V_{max} d/\nu$, where V_{max} is the maximum droplet velocity and ν is the carrier fluid viscosity). This calculation of Re ignores the viscous dissipation due to wall effects[28]. Therefore, to determine the relevant forces in our system, we calculated that the inertial forces are on the order of $\sim 1\,\mu N$, based on experimental data (Supplementary Fig. 2), whereas the magnetic and viscous forces are $\sim 10\,\mu N$ (Supplementary Figs 3–6). Hence, we deduced that the viscous forces dominate over the inertial forces.

The potential wells formed in the '*T* & *I*-bar' geometry do not lie on a straight line (Fig. 2a), resulting in serpentine droplet trajectories (Fig. 2b). Both the trajectories (Fig. 2b) and velocity profiles (Fig. 2c) are reproducible over each 360° cycle of $\mathbf{B}_i$ (Supplementary Movie 2). Independent of the frequency f, the droplets exhibit four velocity (V_x) peaks in each cycle—one for each of the four wells activated at the angles $\varphi = (0°, 90°, 180°, 270°)$. Also, the velocity peaks occur approximately at the same positions (Fig. 2b), which is at a distance $r \sim d/2$ from the edge of each bar acting as a potential well. In our experiments, the droplet size is similar to the size of the well (using the width of bar w as a length scale, $w \sim d$), and thus cannot be considered a point source. Therefore, at $r \sim d/2$, the droplet is tangent to the edge of the bar and the magnitude of the attractive magnetic force reaches a maximum (Supplementary Fig. 3a,b). For $r < d/2$, the portion of the droplet that has passed the centre of the well is pulled back towards the well, thus decreasing the net attractive force on the droplet. As we increase f, the velocity peaks increase in magnitude but are shifted towards larger angles φ (Fig. 2c). Increased viscous drag forces due to higher average droplet velocity $\overline{V} = Sf$ cause the droplet to reach a given position x on the bars at a larger angle φ compared to lower frequencies. As φ is proportional to normalized time tf, with $\varphi(t) = 2\pi ft$, a larger angle φ at a given position x implies that a droplet has a temporal delay.

To quantify the relative angular delay between droplet trajectories at two frequencies f_1 and f_2, we define $\Delta\varphi(x) = \varphi_1 - \varphi_2$, where φ_1 and φ_2 are the corresponding angles of $\mathbf{B}_i$. We measured $\Delta\varphi$ on kymograms of the droplet positions x as a function of angle φ for $f = 3$–15 Hz (Fig. 2d). We observe that one well can incur a delay $\Delta\varphi$ that can be compensated by a subsequent well to maintain synchronicity in the overall cycle. However, with increasing f, we expect droplets to eventually lose their synchronization. For example, $f = 18$ Hz causes the same size droplets ($d = 600\,\mu m$) to arrive at the '*I*-bar' too late and miss the entire cascade (Fig. 3a and

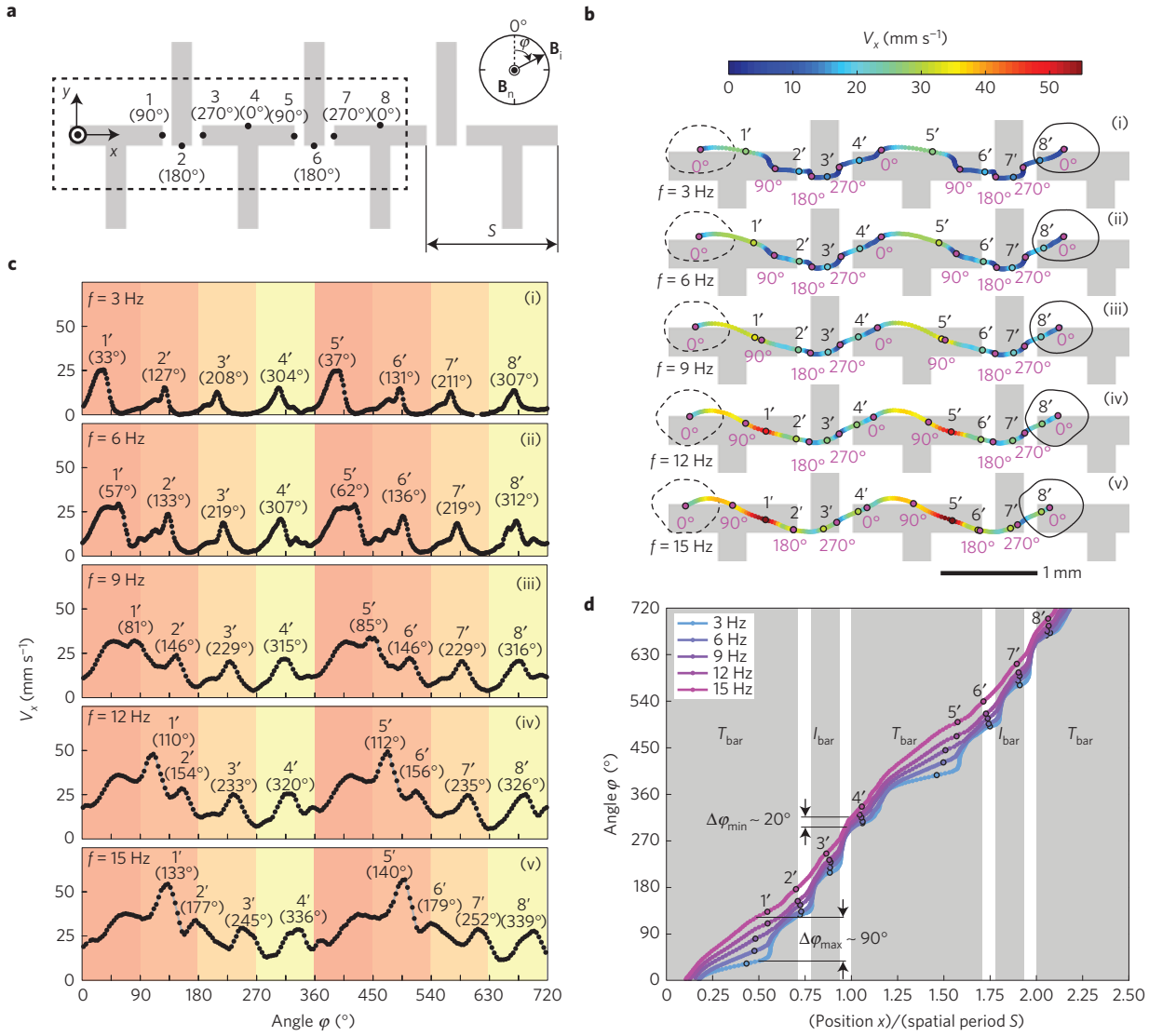

Figure 2 | Synchronous droplet propagation. Experiments with a propagating ferrofluid droplet of diameter $d = 600\,\mu$m (channel height $h = 380\,\mu$m) immersed in silicone oil under a clockwise in-plane rotating field $\mathbf{B}_i$ in the frequency range $f = 3$–15 Hz. **a**, Schematic of potential wells, denoted by numbers (1–8), formed on a periodic track of '*T*' and '*l*' bars, where *S* is the spatial period. The angle φ denotes the instantaneous angular orientation of $\mathbf{B}_i$ and is proportional to normalized time *tf* with $\varphi(t) = 2\pi ft$. The parentheses indicate the angles φ that correspond to each potential well. **b**, Droplet trajectories for $f = 3$–15 Hz (i–v), where the colour represents the magnitude of the horizontal component of velocity V_x. The background has been removed from the images. Purple numbers/circles indicate the four cardinal angles $\varphi = (0°, 90°, 180°, 270°)$. Black numbers in primes (1′–8′) indicate the local V_x maxima that are the responses to the formation of the potential wells denoted by (1–8) in **a**. The trajectories are repeatable over each 360° cycle. **c**, Diagrams of velocity V_x versus φ for $f = 3$–15 Hz (i–v). Black numbers indicate the same V_x maxima shown in **b** and the numbers in the parentheses indicate the angles φ where these maxima occur. The vertical colour bands indicate each quadrant of φ. **d**, Kymograms of position *x* versus φ. Grey bands indicate the '*T*' and '*l*' bars. The angle difference $\Delta\varphi(x) = \varphi_1 - \varphi_2$ between the frequencies $f_1 = 15$ Hz, $f_2 = 3$ Hz for a given position *x* quantifies the relative angular delay between minimum and maximum frequencies. The kymograms diverge midway along the '*T*' bar ($\Delta\varphi_{max} \sim 90°$ at $x/S \sim 0.5$) and then converge at the gap between the '*T* and *l* bars' ($\Delta\varphi_{min} \sim 20°$ at $x/S \sim 0.95$). Therefore, the delay $\Delta\varphi$ incurred by one well can be compensated by a subsequent well, maintaining the synchronicity of the system overall. Experiments performed at $B_i = 40$ G, $B_n = 250$ G. Viscosities $\mu_{drop} = 5$ mPa s, $\mu_{oil} = 4.6$ mPa s.

Supplementary Movie 3). This loss of synchronicity is caused by the delay that started accumulating from the middle of the '*T*-bar' and led to a $\Delta\varphi_{max} \sim 120°$ (comparing $f_1 = 18$ Hz and $f_2 = 3$ Hz, Fig. 3b). If the droplet misses the cascade, it temporarily reverses its motion because $\mathbf{B}_i$ activates wells located upstream. Then, it takes at least a full rotation of $\mathbf{B}_i$ before the droplet re-enters the next well in the cascade after performing a loop.

Simulations and establishment of synchronization limits

Any implementation of cascadable and robust logic operation must be within synchronization limits. To establish these limits, we developed a reduced-order model. The model solves for the droplet's equation of motion, $\mathbf{F}_m + \mathbf{F}_{drag} = m_d \mathbf{a}_d$, where m_d and $\mathbf{a}_d$ are mass and acceleration. We estimated the magnetic force $\mathbf{F}_m$ on the droplet by making a first-order approximation of the '*T*-bars' and '*I*-bars' as a periodic sequence of superposed individual bars[29] (Supplementary Information). The viscous drag force $\mathbf{F}_{drag}$ is dependent on the complex rheology of the ferrofluid, the dynamic shape change of the droplets (Fig. 1g) and the effect of the normal field $\mathbf{B}_n$ on the lubrication film. Because of the difficulty in controlling each of these parameters, we devised a secondary experiment to measure $\mathbf{F}_{drag}$ directly (Supplementary Information).

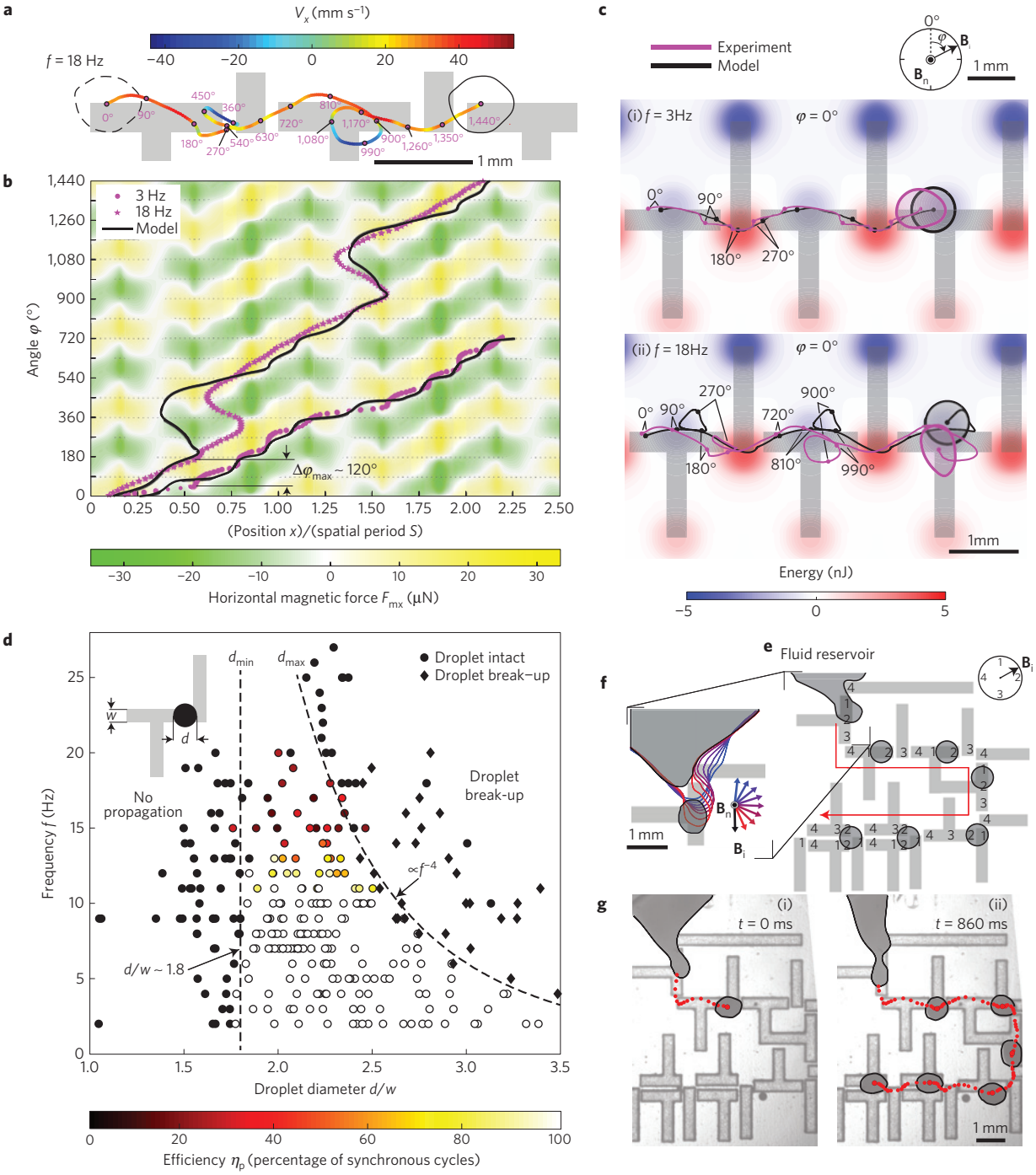

Figure 3 | Characterization of synchronous limits of propagation and synchronous droplet generation. a, Trajectory of droplet of $d = 600\,\mu$m at $f = 18$ Hz where the droplet reverses its motion (Supplementary Movie 3) and performs loops. Purple numbers/circles indicate the angle φ of $\mathbf{B}_i$. **b**, Kymograms of droplet position x versus φ for $f = 3$ Hz and $f = 18$ Hz, where experiments (purple) are juxtaposed with theoretical model predictions (black). The background colour represents the magnitude of horizontal magnetic force F_{mx} across the x-axis calculated by the model for all $(x/S, \varphi)$ combinations, revealing bands of positive ($F_{mx} > 0$, yellow) and negative ($F_{mx} < 0$, green) forces. **c**, Experimental (purple) and modelled (black) trajectories for $f = 3$ Hz (i) and $f = 18$ Hz (ii) (Supplementary Movies 4 and 5). Selected multiples of the cardinal angles of $\varphi = (0°, 90°, 180°, 270°)$ are indicated by dots. **d**, Phase diagram for droplet propagation for $f = 2$–27 Hz, $d = 300$–$1{,}000\,\mu$m and fixed channel height $h = 380\,\mu$m. The colour bar corresponds to the efficiency $\eta_p = (N_t - N_a)/N_t$, where N_t is the number of rotations of the magnetic field $\mathbf{B}_i$ and N_a is the number of loop events where a droplet fails to follow a potential well. **e**, Schematic of '*T* & *I*-bar' arrangement to generate droplets from an adjacent fluid reservoir. The black numbers 1–4 denote the potential wells activated by the angular orientations of $\mathbf{B}_i$, prescribing the droplet trajectories (marked in red). **f**, Experimental time-lapse of droplet generation. The background has been removed from the images. The coloured curves indicate the interface of the deforming reservoir corresponding to the angular orientation of $\mathbf{B}_i$, leading to droplet generation. **g**, Snapshots at $t = 0$ ms (i) and $t = 860$ ms (ii) demonstrating synchronous generation of a single droplet (relative standard deviation of diameter $\sigma_d \sim 2\%$) for every cycle of $\mathbf{B}_i$ at $f = 6$ Hz (Supplementary Movie 14). The background images are presented as semi-transparent. The droplet boundaries and the reservoir interface are marked in black. The droplet trajectories are marked in red. All experiments and simulations performed at $B_i = 40$ G, $B_n = 250$ G.

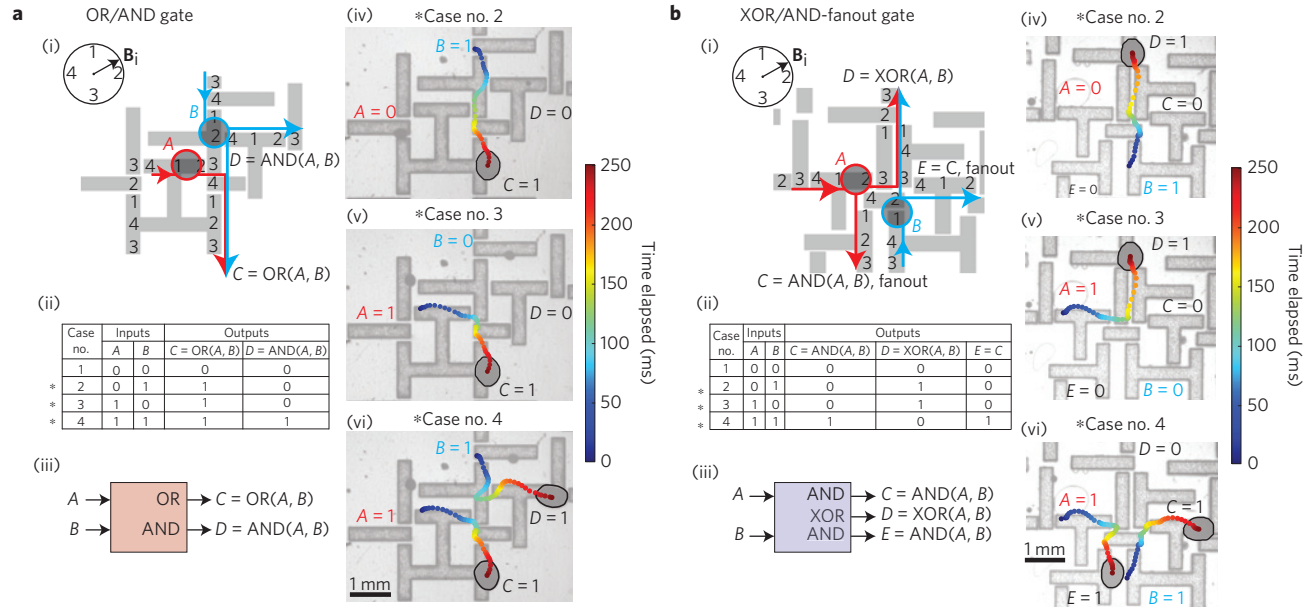

Figure 4 | Combinational droplet logic: basic gates. Logic gates with junction geometries where droplets interact through a repulsive magnetic force to perform logic operations. '1' or '0' is assigned to the presence and absence of a droplet at a given inlet or outlet port of the junction geometry. The junctions act as combinational logic gates; the input droplets at the inlet ports 'compute' the output droplets at the outlet ports. **a**, OR/AND logic gate. (i) Schematic where the black numbers 1–4 denote the potential wells activated by the angular orientations of $\mathbf{B}_i$, prescribing the droplet trajectories (corresponding droplet-trajectory pairs have the same colour). (ii) A truth table. (iii) Block representation of logic gate. (iv–vi) Experimental realizations of logic cases (Supplementary Movie 15), corresponding to the asterisks in (ii). The background images are presented as semi-transparent and the droplet boundaries are marked in black. The colour of the trajectories represents the elapsed time. **b**, XOR/AND-fanout gate (Supplementary Movie 16). Items (i–vi) have the same meanings as in **a**. The XOR is a supercase of logic NOT, for example, for $B=1$, XOR$(A,1)=$NOT(A) shown in cases 2,4 in (v,vi). The XOR/AND-fanout gate has two identical outputs or fanouts, $C=E=$AND(A,B), which, for example, can duplicate input A using $B=1$ so that $C=E=$AND$(A,1)=A$. The XOR/AND-fanout is capable of universal logic—that is, it can be combined to perform any Boolean logic computation. All experiments performed at $f=6$ Hz, $B_i=40$ G, $B_n=250$ G.

Using the model, we calculated $\mathbf{F}_m$ to specify the bounds for synchronous propagation on the kymograms of the droplet positions x as a function of angle φ. The kymogram for $f=3$ Hz lies in the positive magnetic force band ($F_{mx}>0$) and the droplet follows the cascade of potential wells (Fig. 3b). In contrast, the kymogram for $f=18$ Hz enters the negative magnetic force band ($F_{mx}<0$) just as the droplet reverses its motion, then enters a new positive ($F_{mx}>0$) band and the droplet resumes its initial $+x$ direction (Fig. 3b). Furthermore, we solved the droplet's equation of motion and accurately predicted the experimental trajectories. The model accurately captures slope changes in the kymogram for $f=3$ Hz and reproduces the loss of synchronicity and loop behaviour for $f=18$ Hz (Fig. 3c and Supplementary Movies 4 and 5). The model predicts only a single type of loop, whereas two types of loops were observed experimentally.

We explored broader synchronization limits (Fig. 3d) in experiments where we varied both the frequency ($f=2$–27 Hz) and the droplet diameter ($d=300$–$1{,}000$ μm). All other parameters were kept constant, including the droplet and carrier fluid viscosities, interfacial tension, channel height, bar geometry and the magnetic field magnitudes. To quantify the degree of synchronization, we define a droplet propagation efficiency measure $\eta_p=(N_t-N_a)/N_t$, where N_t is the number of rotations of the magnetic field $\mathbf{B}_i$ and N_a is the number of loop events where a droplet fails to follow a potential well. We tested droplets on closed square tracks 'T' and 'I' bars and discovered three modes of operation where perfect synchronization (Supplementary Fig. 7a and Supplementary Movie 6) is compromised: partial synchronization (loop occurrence, Supplementary Fig. 7b and Supplementary Movie 7), no propagation (Supplementary Fig. 7c and Supplementary Movies 8 and 9) and droplet break-up (Supplementary Fig. 7d and Supplementary Movie 10). In particular, perfect synchronization ($n_p=100\%$) occurs at $f\leq 10$ Hz for a range of droplet sizes $d_{min}\leq d\leq d_{max}$ (Fig. 3d). The minimum size limit is independent of frequency $d_{min}\sim 1.8w$, where w is the width of the bar. The maximum limit empirically scales with $d_{max}\propto f^{-4}$ over the range $d_{max}\sim[2.5,3.5]w$. At $f>10$ Hz, only partial synchronization ($n_p<100\%$) is observed; n_p gradually decreases to the point of no propagation. Above d_{max}, droplets tend to break up.

Using the established synchronization limits, we achieved synchronous propagation of multiple droplets of different sizes (Supplementary Fig. 8a and Supplementary Movie 11). Turning off or flipping the direction of $\mathbf{B}_i$ can freeze or reverse the propagation of a droplet (Supplementary Fig. 8b and Supplementary Movie 12). This establishes the requirements for reversibility and non-volatile operation in our system. The density of the droplet circuits can also be increased by having a greater number of wells over the surface area of the fluidic chip. To demonstrate this experimentally, we designed circuits with counter-rotating concentric loops nested inside each other. Counter-rotating circulation (droplets travelling in opposite directions simultaneously) is obtained by mirroring the geometry of the bars (Supplementary Fig. 8c and Supplementary Movie 13).

Aside from achieving synchronous propagation, droplets need to be generated inside the fluidic chip without external control. To address this, we used the 'T & I-bar' arrangement (Fig. 3e) to extract droplets from adjacent fluid reservoirs (Fig. 3f). Utilizing the same clocking mechanism used for droplet propagation—that is, the rotating field $\mathbf{B}_i$—we generated droplets of uniform size (relative standard deviation of droplet diameter, $\sigma_d\sim 2\%$) in a synchronous manner (Fig. 3g and Supplementary Movie 14).

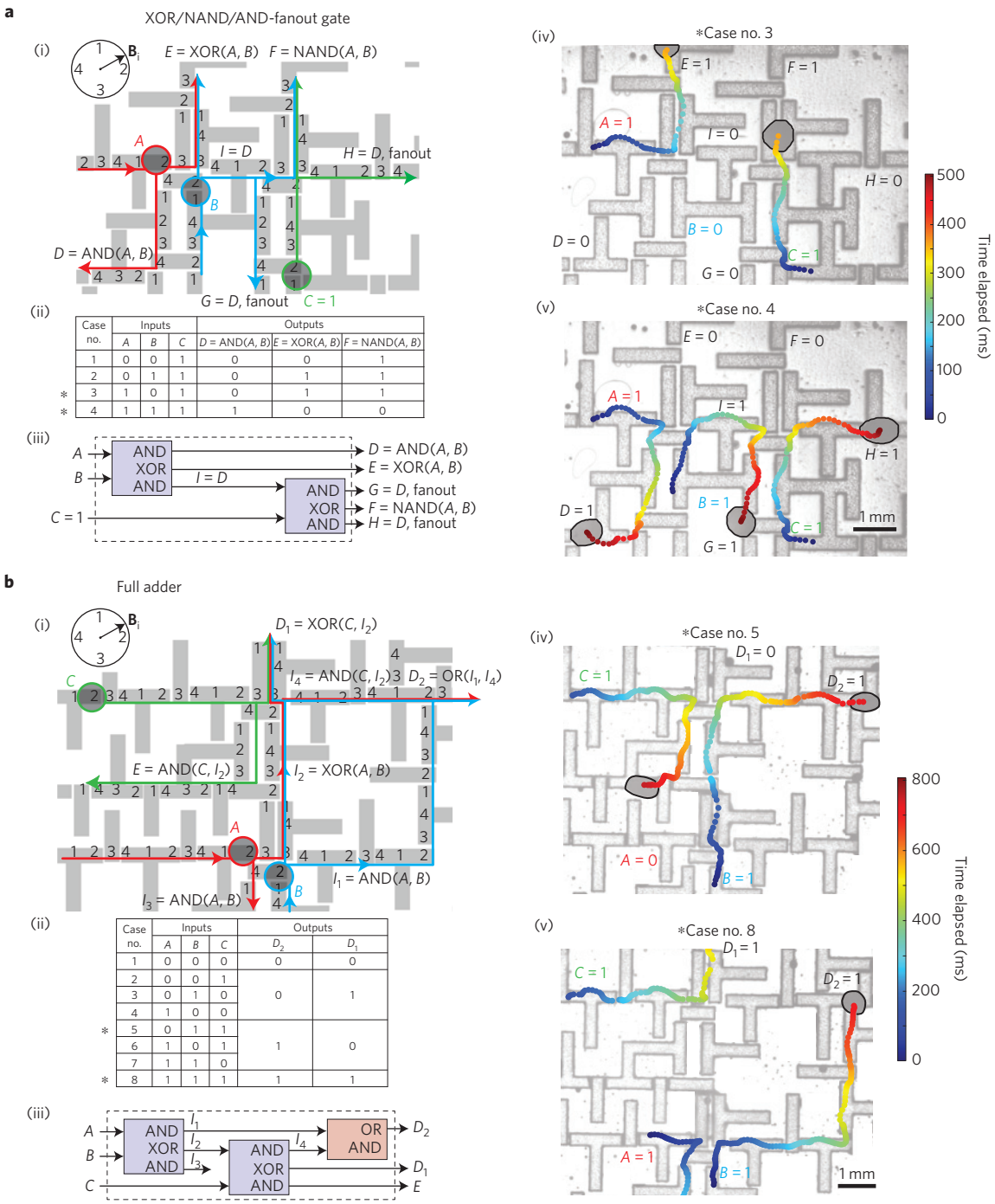

Figure 5 | Combinational droplet logic: composite gates. Logic gates made by combining the gates of Fig. 4. **a**, XOR/NAND/AND-fanout logic gate (Supplementary Movie 17) made by combining two XOR/AND gates. (i) Schematic, where the black numbers 1–4 denote the potential wells activated by the angular orientations of $\mathbf{B}_i$, prescribing the droplet trajectories (corresponding droplet-trajectory pairs have the same colour). (ii) A truth table. (iii) Block representation of logic gate. (iv,v) Experimental realizations of logic cases, corresponding to the asterisks in (ii). The background images are presented as semi-transparent and the droplet boundaries are marked in black. The colour of the trajectories represents the elapsed time. The XOR/AND on the left receives inputs A, B and outputs $I = \mathrm{AND}(A, B)$. The XOR/AND on the right receives inputs I, $C = 1$ and outputs $F = \mathrm{XOR}(I, 1) = \mathrm{NOT}(I) = \mathrm{NAND}(A, B)$. The outputs G, H and the intermediate output I represent fanouts because each duplicates the output D. **b**, Full adder made by combining two XOR/AND-fanout gates and one OR/AND gate. Items (i–v) have the same meanings as in **a**. The full adder receives a maximum of three droplet bits and adds them into the binary sums 00, 01, 10, 11. All experiments performed at $f = 6$ Hz, $B_i = 40$ G, $B_n = 250$ G.

Design of logic gates

After elucidating the synchronization limits of single droplets, we designed logic gates where multiple droplets interact with each other to perform logic operations. A logic gate is defined by a unique junction geometry that receives, at its inlet ports, droplets propagating on different tracks of 'T' and 'I' bars. A magnetic repulsive interactive force (scaling as $F_{m,\mathrm{dipol}} \propto m_1 m_2 r^{-4}$ if we approximate the two droplets as point dipoles with magnetic moments $\mathbf{m}_1$, $\mathbf{m}_2$ at a distance r; ref. 30) prevents the incoming droplets from merging and—based on the junction

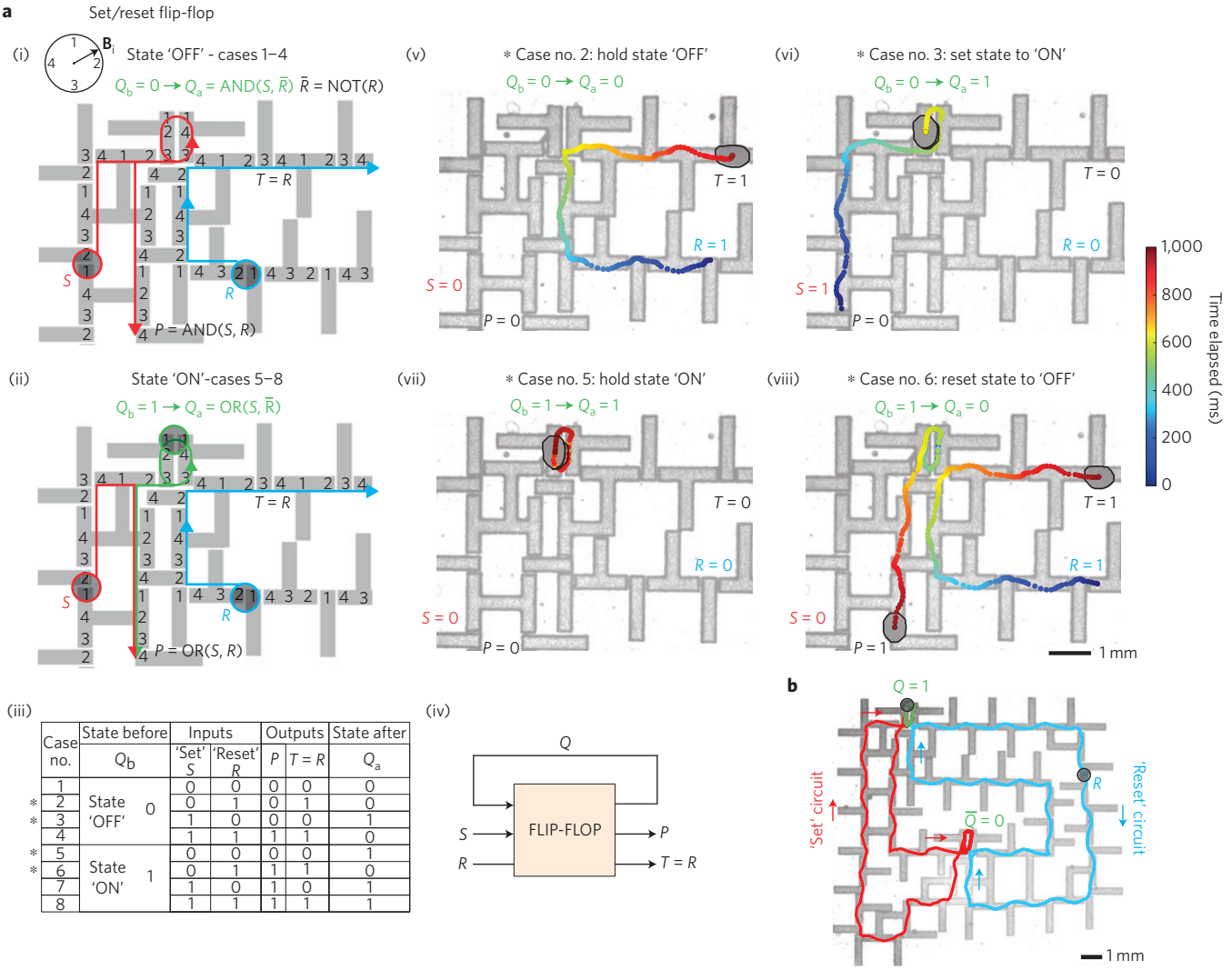

Case no.	State before Q_b	Inputs 'Set' S	Inputs 'Reset' R	Outputs P	Outputs T = R	State after Q_a
1	State 'OFF' 0	0	0	0	0	0
* 2		0	1	0	1	0
* 3		1	0	0	0	1
4		1	1	1	1	0
* 5	State 'ON' 1	0	0	0	0	1
* 6		0	1	1	1	0
7		1	0	1	0	1
8		1	1	1	1	1

Figure 6 | Sequential droplet logic: set/reset flip-flop and fundamental finite-state machine. a, Set/reset flip-flop that can obtain binary states (Supplementary Movie 18) by storing a droplet at a junction geometry ('ON' or $Q=1$) or extracting it ('OFF' or $Q=0$). The junction acts as a sequential logic gate; the outputs depend both on the present inputs and the internal state defined by past inputs. (i,ii) Schematics for states 'ON' and 'OFF', where the black numbers 1–4 denote the potential wells activated by the angular orientations of $\mathbf{B}_i$, prescribing the droplet trajectories (corresponding droplet-trajectory pairs have the same colour). (iii) A truth table. (iv) Block representation of flip-flop. (v–viii) Experimental realizations of logic cases, corresponding to the asterisks in (iii). The background images are presented as semi-transparent and the droplet boundaries are marked in black. The colour of the trajectories represents elapsed time. If the state is already 'OFF', the 'Reset' droplet R has no effect (v). The 'Set' droplet S switches the state to 'ON' ($Q_b=0 \rightarrow Q_a=1$) (vi). The 'ON' state is held if no droplet R enters the junction (vii). Otherwise the state is switched back to 'OFF' ($Q_b=1 \rightarrow Q_a=0$) (viii). **b**, Fundamental finite-state machine made by combining two flip-flops. A 'Reset' droplet provides the stimuli for switching between two states by extracting successively a 'Set' droplet from each flip-flop (Supplementary Movie 19). Red and blue show the trajectories of the 'Set' and 'Reset' droplets, respectively, and green indicates the trajectory of a stored droplet. All experiments performed at $f=6$ Hz, $B_i=40$ G, $B_n=250$ G.

geometry—diverts them to specific outlet ports. The junction thus acts as a combinational[4] logic gate; the input droplets at the inlet ports 'compute' the output droplets at the outlet ports. Because droplet mass is conserved, our logic gates are conservative, with multiple coupled computations occurring in a single junction geometry. We first designed an OR/AND gate (Fig. 4a and Supplementary Movie 15) and an XOR/AND-fanout gate (Fig. 4b and Supplementary Movie 16). As XOR is a superset of logic NOT, the XOR/AND-fanout gate is capable of universal digital logic—that is, it can be combined to perform any Boolean logic operation. In addition, the XOR/AND-fanout gate has two identical outputs or fanouts which can be used to duplicate its inputs.

As droplet propagation is synchronous, multiple logic gates can be combined without asynchronization errors: we thus used the OR/AND and XOR/AND-fanout gates as basic blocks to build cascadable logic gates. Characteristically, we combined two XOR/AND-fanout universal gates to create a NAND gate (Fig. 5a and Supplementary Movie 17), a commonly used universal gate[4]. Furthermore, we combined two XOR/AND-fanout gates and one OR/AND gate to create a full adder (Fig. 5b) that receives a maximum of three droplet bits '1' and adds them into the binary sums 00, 01, 10, 11. To test robustness, all circuits were tested in a ring configuration where the gate outputs were re-routed back as inputs over multiple cycles of logic operations. As shown in Supplementary Movies 15–17, the operations are consistent and highly repeatable (as depicted in overlapping droplet trajectories). Hence, the ring configurations preserve the same logic state, acting as memory loops. If we turn off

the magnetic fields, the droplets are immobilized, preserving their exact position. When the fields are turned on again, the droplets resume the operation, thus making our implementation non-volatile.

To incorporate memory in our logic operations, we designed logic gates that can obtain binary states, by storing a droplet (state 'ON') at a junction geometry or extracting it out (state 'OFF'). This implementation corresponds to sequential logic[4] because the outputs depend both on the present inputs and the internal state defined by past inputs. In particular, we implemented a droplet Set/reset (SR) flip-flop (Fig. 6a and Supplementary Movie 18), which is a fundamental building block for memory. We also used these functions to demonstrate bistability in a simple finite-state machine (Fig. 6b and Supplementary Movie 19). This finite-state machine consists of a closed circuit of a 'Set' droplet that alternates between two flip-flops owing to the interaction with a 'Reset' droplet that propagates on a separate circuit.

Discussion

We postulate that the robustness of synchronous logic ensures the large-scale integration of the presented Boolean logic circuits. Using scaling arguments we showed that our droplet circuits can be scaled down to the sub-nanolitre regime ($d \sim 1$–$10\,\mu$m). According to our current model, the magnetic force scales as $F_m \propto d^2$ (Supplementary Fig. 9) assuming bar dimensions scale down linearly with droplet diameter $d \sim 1$–$1{,}000\,\mu$m. Using a formula for the viscous drag force for Hele-Shaw flow at low capillary numbers[31], we derived $F_m/F_{drag} \propto M_d M_b (d/\sigma)^{1/3} (\mu f)^{-2/3}$ (Supplementary Information), where M_d and M_b are the magnetization of the droplet and the bar, and μ, σ are the carrier fluid's viscosity and interfacial tension. The weak dependence on droplet size thus leaves a wide margin for scaling down the system for the manipulation of thousands of droplets simultaneously.

From a conceptual perspective, the presented logic family has several unique features not usually captured by the faster, ubiquitous electronic logic. First, our system can function in the near-zero clock frequency limit as any given state can be approximated as a quasi-static equilibrium. This gives us full control over the rate at which operations are executed, unlike electronic logic, where operations are generally performed at a fixed clock frequency[4]. Second, energy is delivered to all logic gates by a magnetic field distributed over 3D space, rather than a 2D network of conductive wires. This allows us to distribute energy efficiently and precisely to where it is needed without issues related to impedance losses, thermal hotspots, unintended cross-talk, and routing constraints. Third, because energy delivered to individual gates in a cyclic fashion, a single droplet 'bit' can drive an infinite number of subsequent gates along a track. Thus, the fanout of our logic gates is infinite, whereas electronic logic is limited to a typical fanout of the order of 10 or fewer[4]. Note these features are also missing in asynchronous pressure-based logic systems that use droplets or bubbles[19–22].

External sensing and control can be included using embedded current wires underneath the permalloy bars to provide or detect local magnetic field perturbations[26,32]. The primary magnetic field source (Helmholtz coils) can be easily shrunk using packaging technologies developed for magnetic bubble memory[23]. Furthermore, it is possible to use the same scheme to implement control over inverse non-magnetic droplets, or magnetic holes[33–35] embedded in a ferrofluid or double emulsions, opening the doors for manipulation of any arbitrary fluid.

The capability of synchronous logic-based droplet control enables algorithmic manipulation of materials at the intersection of computer science and fabrication. We predict that the capabilities presented here will enable integrated autonomous parallel droplet manipulation using logic on a large scale in an integrated fashion, analogous to the scaling seen in digital electronics.

Methods

Methods and any associated references are available in the online version of the paper.

Received 17 September 2014; accepted 22 April 2015; published online 8 June 2015

References

1. Zuse, K. *Calculating Space* MIT Technical Translation AZT-70-164-GEMIT (Massachusetts Institute of Technology, 1970).
2. Landauer, R. The physical nature of information. *Phys. Lett. A* **217,** 188–193 (1996).
3. Wheeler, J. A. Information, physics, quantum: The search for links. *Proc. III International Symposium on Foundations of Quantum Mechanics* 354–368 (1989).
4. Floyd, T. *Digital Fundamentals* 10th edn (Prentice Hall, 2008).
5. Chee, M. *et al.* Accessing genetic information with high-density DNA arrays. *Science* **274,** 610–614 (1996).
6. Winfree, E., Liu, F., Wenzler, L. A. & Seeman, N. C. Design and self-assembly of two-dimensional DNA crystals. *Nature* **394,** 539–544 (1998).
7. Mao, C., LaBean, T. H., Reif, J. H. & Seeman, N. C. Logical computation using algorithmic self-assembly of DNA triple-crossover molecules. *Nature* **407,** 493–496 (2000).
8. Teh, S-Y., Lin, R., Hund, L-H. & Lee, A. P. Droplet microfluidics. *Lab Chip* **8,** 198–220 (2008).
9. Garstecki, P., Fuerstman, M. J., Stone, H. A. & Whitesides, G. M. Formation of droplet and bubbles in a microfluidic T-junction-scaling and mechanism of break-up. *Lab Chip* **6,** 437–446 (2006).
10. Schwarz, J. A., Vykoukal, J. V. & Gascoyne, P. R. Droplet-based chemistry on a programmable micro-chip. *Lab Chip* **4,** 11–17 (2004).
11. Song, H., Chen, D. L. & Ismagilov, R. F. Reactions in droplets in microfluidic channels. *Angew. Chem. Int. Ed.* **45,** 7336–7356 (2006).
12. Schneider, T., Kreutz, J. & Chiu, D. T. The potential impact of droplet microfluidics in biology. *Anal. Chem.* **85,** 3476–3482 (2013).
13. Gascoyne, P. R. *et al.* Dielectrophoresis-based programmable fluidic processors. *Lab Chip* **4,** 299–309 (2004).
14. Link, D. R. *et al.* Electric control of droplets in microfluidic devices. *Angew. Chem. Int. Ed.* **45,** 2556–2560 (2006).
15. Ahn, K. *et al.* Dielectrophoretic manipulation of drops for high-speed microfluidic sorting devices. *Appl. Phys. Lett.* **88,** 024104 (2006).
16. Brzobohaty, O., Siler, M., Jezek, J., Jakl, P. & Zemanek, P. Optical manipulation of aerosol droplet using a holographic dual and single beam trap. *Opt. Lett.* **38,** 4601–4604 (2013).
17. Wixforth, A. *et al.* Acoustic manipulation of small droplets. *Anal. Bioanal. Chem.* **379,** 982–991 (2004).
18. Pamme, N. Magnetism and microfluidics. *Lab Chip* **6,** 24–38 (2006).
19. Prakash, M. & Gershenfeld, N. Microfluidic bubble logic. *Science* **315,** 832–835 (2007).
20. Cheow, L. F., Yobas, L. & Kwong, D-L. Digital microfluidics: Droplet based logic gates. *Appl. Phys. Lett.* **90,** 054107 (2007).
21. Cybulski, O. & Garstecki, P. Dynamic memory in a microfluidic system of droplets travelling through a simple network of microchannel. *Lab Chip* **10,** 484–493 (2010).
22. Fuertman, M. J., Gartecki, P. & Whitesides, G. M. Coding/decoding and reversibility of droplet trains in microfluidic networks. *Science* **315,** 828–832 (2007).
23. Chang, H. *Magnetic Bubble Technology: Integrated-Circuit Magnetics for Digital Storage and Processing* (IEEE Press and Wiley, 1975).
24. Romankiw, L., Slusarczuk, M. M. G. & Thompson, D. A. Liquid magnetic bubbles. *IEEE Trans. Magn.* **11,** 25–28 (1975).
25. Donolato, M. *et al.* Magnetic domain wall conduits for single cell applications. *Lab Chip* **11,** 2976–2983 (2011).
26. Lim, B. *et al.* Magnetophoretic circuits for digital control of single particles and cells. *Nature Commun.* **5,** 3846 (2014).
27. White, R. *Viscous Fluid Flow* 3rd edn (McGraw-Hill, 2006).
28. Rabaud, D. *et al.* Manipulation of confined bubbles in a thin microchannel: Drag and acoustic Bjerknes forces. *Phys. Fluids* **23,** 042003 (2011).
29. McCaig, M. & Clegg, A. G. *Permanent Magnets in Theory and Practice* 2nd edn (Pentech Press, 1985).
30. Jiles, D. *Introduction to Magnetism and Magnetic Materials* 2nd edn (CRC Press, 1998).
31. Dangla, R. *2D Droplet Microfluidics Driven by Confinement Gradients* Thesis, Ch. 3 (École Polytechnique 2012).
32. Nguyen, N-T., Ng, K. M. & Huang, X. Maninulation of ferrofluid droplet using planar coils. *Appl. Phys. Lett.* **89,** 052509 (2006).

33. Toussaint, R., Akselvoll, J., Helgesen, G., Skjeltorp, A. T. & Flekkoy, E. G. Interaction model for magnetic holes in a ferrofluid layer. *Phys. Rev. E* **69,** 011407 (2004).
34. Gans, B. J., Blom, C., Philipse, A. P. & Mellema, J. Linear viscoelasticity of an inverse ferrofluid. *Phys. Rev. E* **60,** 4518–4527 (1999).
35. Gans, B. J., Duin, N. J., van den Ende, D. & Mellema, J. The influence of particle size on the magnetorheological properties of an inverse ferrofluid. *J. Chem. Phys.* **113,** 2032–2042 (2000).

Acknowledgements

We acknowledge all members of the Prakash Lab for useful discussions. G.K. is supported by the Onassis Foundation and the A.G. Leventis Foundation. J.S.C. is supported by a grant from the Gordon and Betty Moore Foundation. M.P. is supported by the Pew Foundation, the Moore Foundation, the Keck Foundation, a Terman Fellowship and a NSF Career Award. We acknowledge S. X. Wang and A. El-Ghazaly for providing an alternating gradient magnetometer and helping with measurements of the Permalloy material. We also acknowledge Z. Hossain with regards to the C and Python codes written to obtain and read the data from the embedded microcontrollers.

Author contributions

G.K. and M.P. designed the research and planned the experiments. G.K. performed the micro-fabrication, conducted the experiments and developed image processing tools. G.K. and J.S.C. developed the reduced-order models. G.K. derived the scaling laws and developed the logic gates. All authors analysed the data, interpreted the results and wrote the manuscript.

Additional information

Supplementary information is available in the online version of the paper. Reprints and permissions information is available online at www.nature.com/reprints. Correspondence and requests for materials should be addressed to M.P.

Competing financial interests

A patent has been filed by Stanford University based on ideas presented here (PCT/US2013/056821).

Methods

Fabrication of fluidic chips. The fluidic chips were fabricated using two different methods. The first method used photolithography techniques similar to making PCB boards. Permalloy foil 25 μm thick (Supermalloy C, composition Ni77/Fe14/Cu 5/Mo 4, Goodfellows) were bonded on microscope glass slides 1 mm thick (25 mm side squares), using epoxy glue (3M DP420 Off-white colour). The epoxy was cured for 24 h at room temperature. Positive photoresist (Shipley S-1813, Microchem) was then spin-coated on the samples for 5 s at 900 r.p.m. and for 30 s at 3,000 r.p.m. Then the samples were baked on hot plates at 120 °C for 2 min. To transfer the shapes of the '*T* & *I*-bar' arrangement, transparency masks having a resolution of 8000DPI (Artnet Pro, Santa Clara) were used. Using these masks, the backed samples were exposed to 200 mJ cm^{-2} of collimated light for 14 s. After exposure, the photoresist was developed in Microposit MF-319 developer for 1 min. Next, the sample was rinsed with water to spray out the dissolved photoresist and then hardbaked at 120 °C for 2 min. The samples were etched using ferric chloride (MG Chemicals) at a temperature of 45 to 50 °C for approximately 15 min. Once the patterns were formed, the remaining photoresist was stripped using acetone. A hydrophobic layer of liquid Teflon (DuPont AF601S2106) was spin-coated on the surface of the chip at 1,500 r.p.m. for 30 s. The coatings provide a lubrication film that eliminates contact angle hysteresis in the system. Once the liquid Teflon was spin-coated the sample was cured at 90 °C for 1 h on a hot plate. The second method used a 3W diode-pumped solid state ultraviolet laser cutter (DPSS Lasers). The same permalloy foil as used in the first method was bonded on microscope glass slides, using epoxy glue (Loctite E-30CL). Then, the laser cutter was programmed to etch the foil to transfer the shapes of the '*T* & *I*-bar' arrangement. Next, the permalloy foil was peeled off the glass slide, leaving the '*T* & *I*-bar' shapes. The sample was then cleaned with nitrogen, coated with Teflon, using the same techniques as in the first method. For either of the two fabrication methods, a closed top planar working surface was formed by adding a glass coverslip similarly coated with Teflon. Standard rubber sheets of thickness 0.006 inch (McMaster-Carr) were cut and applied on the surface to create a separation distance.

Electromagnetic coils. The experimental workstation included two custom-built orthogonal Helmholtz coil pairs for the generation of the rotating magnetic field $\mathbf{B}_i$. The fluidic chip was placed at the geometric centre of the coils and was housed within an custom-machined aluminium housing block. Copper tubing (copper alloy 122, internal diameter 0.25 inch, outer diameter 0.19 inch, McMaster-Carr) was wound around the aluminium block with coolant liquid (LIQ-705, Koolant) circulated by an external cooling system (EXT-440CU, Koolant). The coil pairs were driven by a double-output waveform generator (Rigol DG1022) amplified by an audio power amplifier (Samson SX 2400). An oscilloscope (GwInstek, GDS-1152-A-U) was used to observe the signal. The range of the $\mathbf{B}_i$ field is 0 to 100 G for a frequency range of 1 Hz to 100 Hz. A single coil driven by a d.c. power source (Agilent N5770A) was also used for the generation of the bias magnetic field, $\mathbf{B}_n$. The range of the $\mathbf{B}_n$ field is up to 400 G. For all coils, 22-Gauge magnetic wire (McMaster-Carr) with enamel coating providing insulation for up to 390° F was wound by hand. The coils are mounted on modular frames (80/20 Inc). By choosing the ratio $B_n/B_i \geq 5$, the induced magnetic polarity of the droplets was roughly vertical. However, the induced magnetic polarity of the metallic bars is always in-plane as they are too thin to support vertically oriented magnetic domains.

Magnetic field measurements. Magnetic probes were inserted through a hole in the aluminium housing block to measure the magnetic fields just below the centre of the surface of the fluidic chip. Two types of probe were used. The first type was a transverse probe (model MST-410, Lakeshore Technologies), which was connected to a handheld gaussmeter (Model 410 Lakeshore Technologies) providing a real-time readout of $\mathbf{B}_i$ field generated by the Helmholtz coil pair. An axial probe (model MSA-410, Lakeshore Technologies) was also used with the gaussmeter to calibrate the single coil before conducting experiments, measuring the relationship between the current and the $\mathbf{B}_n$ field. The second type of probe consisted of two Hall-effect sensors (SS495A1 Honeywell) placed in an orthogonal arrangement to measure the magnetic field magnitude of each of the orthogonal Helmholtz coil pairs. The angular orientation φ of the $\mathbf{B}_i$ field in the x–y plane was obtained by the measurements of these magnetic fields of each Helmholtz coil pair. The Hall-effect sensors were connected to a microcontroller board (Mega 2560, Arduino) which was programmed to obtain the magnetic field magnitude data and save it to its buffer memory.

Imaging system. Acquisition of the magnetic field data was synchronized with acquisition of video frames of the fluidic chip by triggering a high-speed camera (Phantom v5.0). The camera was mounted on a x–y stage (Thor Labs, PT1) on top of a lab jack (Thor Labs, L490) to provide translation in the x, y, z axes. We used imaging frame rates up to 3,000 fps. A modular infinity microscope (Applied Scientific Instrumentation, MIM system) was used with the camera. A warm white light 500 mW LED source (Thor Labs, MWHCL3) coupled to a fibre optic cable was combined with a collimator lens and a beamsplitter (Edmund Optics, 50R/50T plate) to make a reflection microscope system capable of high-speed video capture. Using infinity-corrected long working distance objectives (Mitutoyo), the system magnification range was from ×1 to ×100 with corresponding resolutions of 11 μm to 0.4 μm.

Fluids. An immiscible solution of water-based ferrofluid droplets (EMG700, Ferrotec) in silicone oil 5 cSt (Sigma Aldrich CAS: 63148-62-9) as carrier fluid, was used. The silicone oil was selected because of its low viscosity, low cost, non-toxicity and its ability to form a non-immiscible solution with the ferrofluid that would prevent any wetting of the latter. Other oils could also have been used, such as perfluorinated oils, which offer the same advantages as the silicone oil and also do not swell PDMS, which is commonly used for microfluidic chips. The optimized combination of working fluids will be investigated in future research endeavours.

Image analysis tools. A custom code was written using Matlab to track the droplets from the raw video data. A brightness threshold was defined and droplets were automatically tracked as low-brightness pixel regions. Multiple droplets were tracked using a nearest-neighbour tracking algorithm. The centroid coordinates as well as other geometric dimensions were extracted from those regions, after eroding and dilating the pixel regions representing the droplets. The centroid coordinates of the droplets were smoothed using a moving-average filter with a span value equal to five. The boundaries of the droplets were derived by interpolating splines on the edges of the pixel regions representing the droplets. The asynchronization events (loop occurrences) were automatically detected by comparing the actual travel distance of the droplet to the expected distance.